Available online at www.sciencedirect.com
ScienceDirect
Journal of Computational Physics 227 (2008) 2743–2757
JOURNAL OF COMPUTATIONAL PHYSICS
www.elsevier.com/locate/jcp

An implicit finite element solution of thermal flows at low Mach number

Weiming Liu *, Georgy Makhviladze

Centre for Research in Fire and Explosion Studies, University of Central Lancashire, Preston PR1 2HE, UK

Received 14 May 2007; received in revised form 23 October 2007; accepted 26 October 2007
Available online 17 November 2007

Abstract

Thermal flows at low Mach numbers are a basic problem in combustion, environmental pollution prediction and atmospheric physics areas. Most of the existing schemes for solving this problem treat convection explicitly, which confines time step width due to the CFL condition. In this paper, based on the pseudo residual-free bubble approach [F. Brezzi, L.P. Franca, T.J.R. Hughes, A. Russo, $b = \int g$, Methods Appl. Mech. Eng. 145 (1997) 329–339; T.J.R. Hughes, Multiscale phenomena: Green's functions, the Dirichlet-to-Neumann formulation, subgrid scale models, bubbles and the origins of stabilised methods, Method. Appl. Mech. Eng. 127 (1995) 387–401], we introduce an implicit finite element scheme for the thermal flow problem. We firstly give a low Mach number asymptotics of compressible Navier–Stokes equations for the thermal flows and then derive the numerical scheme for them in detail. Three representative case studies are used to investigate and to test the numerical performances of the proposed scheme.
© 2007 Elsevier Inc. All rights reserved.

Keywords: Thermal flows; Low Mach number; Finite element method; Implicit method; Stabilised finite element method

1. Introduction

Many computational schemes for solving low Mach number flows are obtained by the preconditioning techniques which extend the numerical methods for high Mach number flows into the low Mach number flow computations, for instance, see works [21,22,26–28]. These schemes firstly reduce the Navier–Stokes equations using Turkel preconditioning technique [26] and then are constructed based on Godunov-type method. Some of them employ implicit upwind scheme, e.g. [22]. These schemes do not completely decouple the acoustic modes from the vorticity and entropy modes. They may be the best option to compute the low Mach number flow fields with some part of moderate or high Mach number flows. For the entire flow field with low Mach number, however, these methods are still expensive in computation [14].

* Corresponding author. Tel.: +44 1772 893239.
E-mail address: wliu1@uclan.ac.uk (W. Liu).

0021-9991/$ - see front matter © 2007 Elsevier Inc. All rights reserved.
doi:10.1016/j.jcp.2007.10.025

The acoustic mode separation approach that applies a low Mach number asymptotic ansatz may relax the harsh term of the CFL condition due to the sound speed. Using the low Mach number asymptotic ansatz we can obtain a set of simplified Navier–Stokes equations for the low Mach number flows [17,20]. As usual the obtained simplified equations are integrated temporally by predictor–corrector or fractional step schemes, such as SIMPLE and projection methods, and other methods [11,14,16–18,20,24]. In some works these methods are called the segregated. A common feature for these schemes is that they explicitly treat the convection term and implicitly calculate the pressure and diffusion term. Thus the CFL condition with convection velocity is still an obstacle to restrict time step width. Therefore, in this paper, we introduce an implicit finite element algorithm to solve the low Mach number thermal flows. In addition the proposed scheme which is different from the traditional segregated methods solves a set of completely coupled equations for the velocity, pressure and temperature components to improve the numerical performance.

The content of this paper is as follows. Section 2 describes the governing equations. In Section 3 we give derivation of the algorithm. Section 4 reports the numerical tests to the proposed algorithm. Finally the conclusions are summarised in Section 5.

2. Governing equations

Let Ω and $(0,T)$ be a spatial and temporal domain, and $x \in \bar{\Omega}$ (the set closure of the spatial domain) and $t \in [0,T]$ are the associated coordinates. The Navier–Stokes equations for compressible flows may be written in dimensionless form as

$$\frac{\partial \rho}{\partial t} + (u \cdot \nabla)\rho + \rho \nabla \cdot u = 0, \quad \text{on } \Omega \times (0,T), \tag{1}$$

$$\rho \frac{\partial u}{\partial t} + \rho(u \cdot \nabla)u + \nabla p - \frac{1}{Fr^2}\rho g - \frac{1}{Re}\left\{\nabla^2 u + \frac{1}{3}\nabla(\nabla \cdot u)\right\} = 0, \quad \text{on } \Omega \times (0,T), \tag{2}$$

$$\rho \frac{\partial T}{\partial t} + \rho(u \cdot \nabla)T + (\gamma - 1)M^2 \frac{\mathrm{d}p}{\mathrm{d}t} - \frac{1}{RePr}\nabla^2 T - M^2 \frac{\gamma - 1}{\mathrm{Re}}\Phi - q = 0, \quad \text{on } \Omega \times (0,T) \tag{3}$$

and the state equation,

$$\gamma M^2 p = \rho T, \quad \text{on } \Omega \times (0,T), \tag{4}$$

where $u, \rho, T, p, \gamma, \Phi$ and g denote, respectively, the dimensionless velocity vector, density, temperature, pressure, ratio of specific heats, dissipation function and gravity vector. The term q in (3) is the heat source which can be produced by the reaction or radiation. In this work our major focus is on the numerical scheme for low Mach number flows, hence the heat source is treated as the prescribed. It should be pointed out that such treatment does not affect the scheme introduced in this work and could be applied to reaction flows.

The above equations are obtained by means of non-dimensionalising the compressible equations using $x = \frac{\tilde{x}}{x_{\mathrm{ref}}}, t = \frac{\tilde{t}u_{\mathrm{ref}}}{x_{\mathrm{ref}}}, u = \frac{\tilde{u}}{u_{\mathrm{ref}}}, \rho = \frac{\tilde{\rho}}{\rho_{\mathrm{ref}}}, T = \frac{\widetilde{T}}{T_{\mathrm{ref}}}$ and $p = \frac{\tilde{p}}{\rho_{\mathrm{ref}} u_{\mathrm{ref}}^2}$. The dimensionless numbers appearing in (1)–(4) are defined as

Mach number	Reynolds number	Froude number	Prandtl number
$M = \frac{u_{ref}}{\sqrt{R\gamma T_{ref}}}$	$\mathrm{Re} = \frac{\rho_{ref} u_{ref} x_{ref}}{\mu}$	$Fr = \frac{u_{ref}}{\sqrt{x_{ref}\lVert\vec{g}\rVert}}$	$\mathrm{Pr} = \frac{\mu c_p}{\kappa}$

where μ, k, R and c_p are the dynamic viscosity, thermal conductivity, universal gas constant and specific heat at constant pressure, respectively.

2.1. Low Mach number asymptotics

Now we describe the low Mach number approximate form of the Eqs. (1)–(4), using an asymptotic ansatz based on the little parameter $\alpha = \gamma M^2 \ll 1$. The unknown variables are first expended into the following series:

$$u = u_0 + \alpha u_1 + \cdots, \tag{5}$$
$$\rho = \rho_0 + \alpha \rho_1 + \cdots, \tag{6}$$
$$T = T_0 + \alpha T_1 + \cdots, \tag{7}$$
$$p = \frac{1}{\alpha} p_0 + p_1 + \cdots. \tag{8}$$

Substituting (5)–(8) into (1)–(4) and collecting the same order terms of α, we have

$$\frac{\partial \rho_0}{\partial t} + (u_0 \cdot \nabla)\rho_0 + \rho_0 \nabla \cdot u_0 = 0, \quad \text{on } \Omega \times (0, T), \tag{9}$$
$$\rho_0 \frac{\partial u_0}{\partial t} + \rho_0 (u_0 \cdot \nabla) u_0 + \nabla p_1 - \frac{1}{Fr^2} \rho_0 g - \frac{1}{Re} \left\{ \nabla^2 u_0 + \frac{1}{3} \nabla (\nabla \cdot u_0) \right\} = 0, \quad \text{on } \Omega \times (0, T), \tag{10}$$
$$\rho_0 \frac{\partial T_0}{\partial t} + \rho_0 (u_0 \cdot \nabla) T_0 + \frac{\gamma - 1}{\gamma} \frac{\mathrm{d} p_0}{\mathrm{d} t} - \frac{1}{RePr} \nabla^2 T_0 - q = 0, \quad \text{on } \Omega \times (0, T), \tag{11}$$
$$\nabla p_0 = 0, \quad \text{on } \Omega \times (0, T), \tag{12}$$
$$p_0 = \rho_0 T_0, \quad \text{on } \Omega \times (0, T). \tag{13}$$

Eqs. (9)–(13) are called low Mach number asymptotic equations, in which the pressure is split into spatially uniform thermodynamic pressure and hydrodynamic pressure. The thermodynamic pressure is constant for an open system. When the computational domain is enclosed, it is generally time-dependent. Considering that the total mass in an enclosed system remains invariable, we have [14]

$$p_0 = \frac{\int \rho_0 \, \mathrm{d} V}{\int \frac{1}{T_0} \, \mathrm{d} V}. \tag{14}$$

Based on combination of the above equations we suggest some computational strategies. With the aid of the numerical tests, however, we found that the use of the continuity Eq. (9) does not provide a favorable property for the proposed numerical scheme. In order to seek a set of equations with better convergent behavior we derive a volume equation of fluids to replace it. Combining Eqs. (9) and (11), and further using the equation of state (13), we obtain an equation for the flow divergence

$$\nabla \cdot u_0 - \frac{1}{p_0 RePr} \nabla^2 T_0 = \frac{\gamma - 1}{\gamma p_0} q - \frac{1}{\gamma p_0} \frac{\mathrm{d} p_0}{\mathrm{d} t}, \quad \text{on } \Omega \times (0, T). \tag{15}$$

Eq. (15) shows the variation of the fluid particle volume due to the heat transfer or/and the change of the thermodynamic pressure. For the isothermal steady flows without heat sources, the fluid volume is invariable, therefore, $\nabla \cdot u_0 = 0$.

Now we use the Eq. (15) to replace (9), and thus complete the basic mathematic equations for low Mach number flows, (10)–(15). For the sake of simplification of symbols, we drop out the subscript *0* of the variables in the above equations; p denotes the hydrodynamic pressure and p_0 the thermodynamic pressure.

Comparing the above mathematic model with the model of the projection method, [19], in which the state equation is discarded and the continuity equation and an equation which is similar to (15) are retained, we may further study the difference between the proposed numerical method in this work and segregated methods.

2.2. Initial and boundary conditions

The initial conditions are the velocity, density, pressure and temperature fields at $t = 0$, which are defined by

$$u = u(x), \quad \rho = \rho(x), \quad p = p(x) \quad \text{and} \quad T = T(x), \qquad \text{on } \bar{\Omega}. \tag{16}$$

The boundary conditions are divided into hydrodynamic boundary conditions and thermodynamic boundary condition. The hydrodynamic boundary conditions are posed into

$$u = f, \quad \text{on } \Gamma_1 \quad \text{and} \quad -p + n \cdot \sigma = g, \quad \text{on } \Gamma_2, \tag{17}$$

where $\Gamma = \Gamma_1 \cup \Gamma_2$ and σ denote, respectively, the boundary surfaces and the shear stress tensor. The values of f and g are prescribed and n the unit normal vector, while the thermodynamic boundary conditions are defined as

$$T = h, \quad \text{on } \Gamma_3 \quad \text{and} \quad \frac{\partial T}{\partial n} = \chi, \quad \text{on } \Gamma_4, \tag{18}$$

where $\Gamma = \Gamma_3 \cup \Gamma_4$ and h and χ are the prescribed function. Note that the computation procedure does not require the boundary condition for density, because the density will be evaluated from the equation of state (13) at each time step.

3. Numerical methods

We seek the finite element solution of the Eqs. (10)–(18). The equal-order trilinear interpolation on hexahedral element and/or the linear interpolation on tetrahedral element are used for discretization of the velocity, pressure and temperature, respectively. As is well known, the standard Galerkin formulation for these elements will lead to two kinds of instabilities. One is that the presence of convection terms of the momentum and energy equations may result in spurious oscillations when the Reynolds number of flow is high and the computational mesh is not fine enough. The second instability stems from the inappropriate combination of interpolation functions for the velocity and pressure. This combination violates the Babuska–Brezzi condition for the saddle point problem [3]. As a consequence, it would lead to the so-called spurious pressure modes.

3.1. Stabilised finite element formulation

Theoretically the both instabilities can be viewed as a result of the loss of some small-scale solution during discretizing the equations [13]. If the discrete equations are conversely reformulated into continuous ones, we would see that the reformulated continuous equations have some property which is different from the original equations [15]. Therefore, the stabilized method is to re-capture the lost small-scale solutions during computation by extending the finite element space. Below we will derive a stabilized formulation by means of applying the pseudo residual-free bubble approach, [4,5,8–10,13].

We assume that the Eqs. (10), (11) and (15) are linearised and the density is viewed as a given quantity. In practical computations, however, the density will be updated by the equation of state (13) at each iteration. In addition, for the sake of simplifying symbols we use below an operator to express the above equations. Let L denote the operator of (10), (11) and (15), i.e.

$$L = \begin{pmatrix} \rho\frac{\partial}{\partial t} + \rho u\cdot\nabla - \frac{1}{Re}\left(\nabla^2 + \frac{1}{3}\nabla\cdot\nabla\right) & \nabla & 0 \\ \nabla\cdot & 0 & -\frac{1}{p_0 RePr}\nabla^2 \\ 0 & 0 & \rho\frac{\partial}{\partial t} + \rho u\cdot\nabla - \frac{1}{RePr}\nabla^2 \end{pmatrix}. \tag{19}$$

Using this operator, the Eqs. (10), (11) and (15) may be rewritten as

$$L(S) \equiv L\begin{pmatrix} u \\ p \\ T \end{pmatrix} = F \equiv \begin{pmatrix} \frac{1}{Fr^2}\rho g \\ \frac{\gamma-1}{\gamma p_0}q - \frac{1}{\gamma p_0}\frac{\mathrm{d}p_0}{\mathrm{d}t} \\ q \end{pmatrix}. \tag{20}$$

The trial function spaces of the standard finite element method, $U^h = \left(U_u^h, U_p^h, U_T^h\right)$, are defined as

$$U_u^h = \{u^h | u^h \in (H^{1h})^3, u^h = f, \text{on } \Gamma_1\}, \tag{21}$$

$$U_p^h = \{p^h | p^h \in H^{1h}\}, \tag{22}$$

$$U_T^h = \{T^h | T^h \in H^{1h}, T^h = h, \text{on } \Gamma_3\} \tag{23}$$

and the test function spaces, $V^h = \left(V_u^h, V_p^h, V_T^h\right)$, as

$$V_v = \{v^h | v^h \in (H^{1h})^3, v^h = 0, \quad \text{on } \Gamma_1\}, \tag{24}$$

$$V_q = \{q^h | q^h \in H^{1h}\}, \tag{25}$$

$$V_R = \{R^h | R^h \in H^{1h}, R^h = 0, \quad \text{on } \Gamma_3\}, \tag{26}$$

where $H^{1h} = \{\varphi^h | \varphi^h \in C^0(\bar{\Omega}), \varphi^h|_{\Omega^e} \in P^1 \ \forall \Omega_e \in D\}$ and P^1 and D denote the first order polynomials and the set of the finite element discretization of the domain Ω.

According to the pseudo residual-free bubble approach, the space U^h is enlarged as $U = U^h \oplus U^b$, where $U^b = \oplus_e U_e^B$, and U_e^B is the space of bubble in the element, E. This means that the values of functions from the function spaces are taken zero on the element boundary, that is,

$$U_e^B = (H_0^3(E), H_0^1(E), H_0^1(E)). \tag{27}$$

Thus, the variational formulation of the problem (10)–(18) can be written as;
Find $S = S^h + S^b \in U(S^h \in U^h, S^b \in U^b)$ such that for all $v^h \in V^h$ and $v_b^h \in U^b$,

$$(L(S^h), v^h) + (L(S^b), v^h) = (F, v^h), \tag{28}$$

$$(L(S^h), v_b^h) + (L(S^b), v_b^k) = (F, v_b^h). \tag{29}$$

Due to the bubble function property, the second term on left hand side of (28) has the relation

$$(L(S^b), v^h) = (S^b, L^*(v^h)), \tag{30}$$

where L^* is the formal adjoint of L on E. Furthermore, due to (27) and (29) we have

$$\begin{cases} L(S^b) = -\{L(S^h) - F\} & \text{in } E, \\ S^b = 0 & \text{on } \partial E. \end{cases} \tag{31}$$

Let L^{-1} denote the negative inverse of the operator defined by (31), so that

$$S^b = L^{-1}(L(S^h) - F). \tag{32}$$

Substituting (32) and (30) into (28), we have

$$(L(S^h), v^h) + (L^{-1}(L(S^h) - F), L^*(v^h)) = (F, v^h). \tag{33}$$

Due to the linear interpolation function on element, $L(S^h) - F$ and $L^*(v^h)$ are constants in each element E. Therefore the second term on left hand side of (33) can be written as

$$\begin{aligned} (L^{-1}(L(S^h) - F), L^*(v^h))|_E &= [(L(S^h) - F)|_E][L^*(v^h)|_E][(L^{-1}(1), 1)] \\ &= \frac{1}{|E|} \int_E L^{-1}(1) \mathrm{d}E \int_E (L(S^h) - F) L^*(v^h) \mathrm{d}E = \tau \int_E (L(S^h) - F) L^*(v^h) \mathrm{d}E. \end{aligned} \tag{34}$$

Summarising up the above derivation we obtain the stabilised variational formulation for (10)–(18):
Find $S^h \in U^h$ such that for all $v^h \in V^h$

$$(L(S^h), v^h) + \tau((L(S^h) - F), L^*(v^h)) = (F, v^h), \tag{35}$$

where $\tau = \frac{1}{|E|} \int_E L^{-1}(1) \mathrm{d}E = \frac{1}{|E|} \int_E b_E \mathrm{d}E$ and b_E is a solution of the following problem in E:

$$\begin{cases} L(b_E) = 1 & \text{in } E \\ b_E = 0 & \text{on } \partial E \end{cases} \tag{36}$$

Now we expand (35) and rewrite it as:
Find $u^h \in U_u^h, T^h \in U_T^h$ and $p^h \in U_p^h$ such that

$$\begin{aligned}
&\int_\Omega v^h \cdot \rho\left(\frac{\partial u^h}{\partial t} + u^h \cdot \nabla u^h\right) \mathrm{d}\Omega - \int_\Omega \nabla v^h : p^h \,\mathrm{d}\Omega + \int_\Omega \nabla v^h : \sigma \,\mathrm{d}\Omega + \int_\Omega \left(q^h \nabla \cdot u^h + \frac{1}{p_0 \mathrm{RePr}} \nabla q^h \cdot \nabla T^h\right) \mathrm{d}\Omega \\
&+ \int_\Omega R^h \cdot \rho\left(\frac{\partial T^h}{\partial t} + u^h \cdot \nabla T^h\right) + \frac{1}{RePr} \int_\Omega \nabla R^h \cdot \nabla T^h \,\mathrm{d}\Omega + \sum_{e=1}^{n_{\text{element}}} \int_{\Omega^e} \delta \left\{ (u^h \cdot \nabla) v^h + \frac{1}{\rho} \nabla q^h \right. \\
&\left. - \frac{1}{Re}\left[(\nabla^2 v^h) + \frac{1}{3}\nabla(\nabla \cdot v^h)\right]\right\} \cdot \left\{\rho\left(\frac{\partial u^h}{\partial t} + u^h \cdot \nabla u^h\right) + \nabla p^h - \frac{1}{Re}\left[(\nabla^2 u^h) + \frac{1}{3}\nabla(\nabla \cdot u^h)\right]\right\} \mathrm{d}\Omega \\
&+ \sum_{e=1}^{n_{\text{element}}} \int_{\Omega^e} \varepsilon \left[\nabla \cdot v^h - \frac{1}{p_0 RePr}(\nabla^2 R^h)\right] \cdot \left[\nabla \cdot u^h - \frac{1}{p_0 RePr}(\nabla^2 T^h)\right] \mathrm{d}\Omega \\
&+ \sum_{e=1}^{n_{\text{element}}} \int_{\Omega^e} \phi \left[(u^h \cdot \nabla) R^h - \frac{1}{RePr}(\nabla^2 R^h)\right] \cdot \left[\rho\left(\frac{\partial T^h}{\partial t} + u^h \cdot \nabla T^h\right) - \frac{1}{RePr}\nabla^2 T^h\right] \mathrm{d}\Omega \\
&= \int_{\Gamma_1} v^h \cdot g \,\mathrm{d}\Gamma + \frac{1}{p_0 RePr} \int_{\Gamma_3} q^h \cdot h \,\mathrm{d}\Gamma + \int_\Omega q^h \left(\frac{\gamma - 1}{\gamma p_0} q - \frac{1}{\gamma p_0}\frac{\mathrm{d}p_0}{\mathrm{d}t}\right) \mathrm{d}\Omega + \int_{\Gamma_3} R^h h \,\mathrm{d}\Gamma + \int_\Omega R^h q \,\mathrm{d}\Omega \\
&- \sum_{e=1}^{n_{\text{element}}} \int_{\Omega^e} \delta \left\{ (u^h \cdot \nabla) v^h + \frac{1}{\rho}\nabla q^h - \frac{1}{Re}\left[(\nabla^2 v^h) + \frac{1}{3}\nabla(\nabla \cdot v^h)\right]\right\} \cdot \frac{1}{Fr} \rho g \,\mathrm{d}\Omega \\
&- \sum_{e=1}^{n_{\text{element}}} \int_{\Omega^e} \varepsilon \left[\nabla \cdot v^h - \frac{1}{p_0 RePr}(\nabla^2 R^h)\right] \cdot \left[\frac{\gamma - 1}{\gamma p_0} q - \frac{1}{\gamma p_0}\frac{\mathrm{d}p_0}{\mathrm{d}t}\right] \mathrm{d}\Omega \\
&- \sum_{e=1}^{n_{\text{element}}} \int_{\Omega^e} \phi \left[(u^h \cdot \nabla) R^h - \frac{1}{RePr}(\nabla^2 R^h)\right] \cdot q \,\mathrm{d}\Omega \quad \forall v^h \in V_v^h \ \forall q^h \in V_q^h \ \forall R^h \in V_R^h,
\end{aligned} \tag{37}$$

where σ is the stress tensor excluding the pressure p^h (the hydrodynamic pressure and the thermodynamic pressure). Note that ∇v^h in (37) is also a tensor of order two. A similar approach was applied to convection–diffusion problem in [5]. In the Eq. (37) there are three stabilization parameters: δ, ε and ϕ. They are all the local parameters for each element. Their exact calculations need to solve the local problem (36) on each element. In practical computations of constant-density flows, however, they are always evaluated approximately. As an approximation these schemes are used in this work to evaluate the stabilization parameters. Hence in this work we choose three types of the stabilized parameters for our problems:

First type of the stabilization parameters follows from [25]

$$\begin{cases} \delta = \phi = \frac{h}{2\|u^h\|}\zeta(Re^u), \\ \varepsilon = 0. \end{cases} \tag{38}$$

Second type of the stabilization parameters is proposed by [7]

$$\begin{cases} \delta = \phi = \frac{h}{2\|u^h\|}\zeta(Re^u), \\ \varepsilon = \lambda\|u^h\| h \zeta(Re^u). \end{cases} \tag{39}$$

Third type of the stabilization parameters is suggested by [6]

$$\begin{cases} \delta = \phi = \left[\left(\frac{2}{\Delta t}\right)^2 + \left(\frac{2\|u^h\|}{h}\right)^2 + 9\left(\frac{4\nu}{h^2}\right)^2\right]^{-\frac{1}{2}}, \\ \varepsilon = \lambda \frac{h^2}{\delta}, \end{cases} \tag{40}$$

where h and u^h denote the element length and local velocity, Re^u is the local Reynolds number and λ is a coefficient, which is taken as *0.5* in this work. The function, $\zeta(x)$, is defined as

$$\zeta(x) = \begin{cases} \frac{x}{3}, & 0 \leqslant x \leqslant 3, \\ 1, & 3 \leqslant x. \end{cases} \tag{41}$$

3.2. Spatial discretizations

The spatial discretisation of (37) yields a set of linearised ordinary differential equations:

$$(M + M')\frac{\mathrm{d}S}{\mathrm{d}t} + [N(S_0) + N'(S_0)]S + (K + K')S = F + F', \tag{42}$$

where S_0 expresses the flow state at some time step and $\frac{\mathrm{d}S}{\mathrm{d}t}$ denotes the time derivative of unknown vector; M is the mass matrix and M' is the corrected mass matrix to extend the finite element space; $N(S_0)$ and $N'(S_0)$ denote, respectively, convection matrix and its correction that is actually the SUPG (streamline-upwind/Petrov–Galerkin) term for the momentum Eq. (10) and energy Eq. (11). The matrix $N'(S_0)$ still includes the PSPG (pressure-stabilizing/Petrov–Galerkin) matrix in the volume Eq. (15). The matrix K consists of, respectively, the pressure matrix and viscous matrix of the momentum equation, the divergent matrix and heat-conductive matrix of the volume Eq. (15), and the heat-conductive matrix of the energy equation. Note that the pressure matrix is actually the transpose of the divergent matrix. Owing to linear interpolation element, K' is only the Laplace matrix in the volume equation. Finally, F and F' express the integrations in the right hand side of (37).

3.3. Time integration algorithm

The second order trapezoidal method is applied to solve (42), therefore the whole time integration procedure reads

Give the time step width Δt *and flow state* S_n *at* $t = t_n$
  Do Newton non-linear iteration
    Do linear system solver
    Calculate $R = (M + M')\frac{S_n}{2\Delta t} + \frac{1}{2}[N(S_n) + N'(S_n)]S_n + \frac{1}{2}(K + K')S_n - F_n - F'_n$
    Solve $\left\{\frac{M+M'}{2\Delta t} + \frac{1}{2}[N(S_n) + N'(S_n)] + \frac{1}{2}(K + K')\right\}S_{n+1} + R = 0$
    End Do linear system solver
  Newton non-linear update
  End Do Newton non-linear iteration
Time update and start next time step

The geometrical multigrid preconditioned Krylov iterative method is used for solving the discrete linear algebraic systems in each time step [1].

4. Numerical tests

In this section we choose three typical thermal flows of low Mach number, lid-driven cavity with vertically heated wall, thermal convection induced by fire in a compartment and Rayleigh–Benard flows, to investigate and to test the proposed numerical scheme. All these are three-dimensional flows. We assume that the initial conditions are a static state of the air with the temperature 300 K, density 1.2 kg m^{-3} and atmospheric pressure 1.03×10^5 N m^{-2}, if no other claim is given.

As mentioned in Section 3.3 the numerical solution procedure involves two iterations: Newton non-linear iteration and linear system iteration, see [1]. The linear system solver's iterations do not exceeded 45 to achieve convergent tolerance which is set to 10^{-5} in the following computations. The tolerance for the non-linear iteration is set to 10^{-3}. It is generally achieved by 4 Newton non-linear iterations.

4.1. Lid-driven cavity

The computed cavity consists of a cube with unity sides, which is uniformly meshed by $35 \times 35 \times 35$ hexahedral elements. On the top face the driven boundary condition is posed, namely, a unity velocity drives the flow in the cavity. The boundary condition for the temperature of the lid was 300 K. The other faces are

specified as wall boundary conditions. Two different types of flows were considered: quasi-isothermal flow and asymmetric vertical thermal convection. The type of flow was determined by the boundary conditions on the side wall. For the quasi-isothermal flow, all wall are adiabatic, while for the vertical thermal convection, temperature of the side upstream wall is constant and higher than 300 K (the heated wall), and the boundary conditions on the other faces are the same as the quasi-isothermal flow.

When implementing the driven boundary condition, one should carefully handle the four edges of the top face. They belong to both the side walls and the driving face. If the edges are set into the driving boundary conditions, the computational stability could be significantly damaged.

4.1.1. Quasi-isothermal flow

Firstly we present the isothermal flow computation. The flow Reynolds number is set to 1000. Our computation produced a reasonable solution for this problem. However we also notice a small difference between our results and those published for the 2D flows, see Table 1. There are twofold reasons resulted in the difference. One is that our computation is 3D but the computations in [2,12] are 2D. The other reason is in mesh resolution. The mesh resolution in [2] is almost five times higher than in this work in a 2D cross-section.

Also from Table 1 we can see that the differences of the computational results for three parameters (38)–(40) are minor. This observation is further confirmed by Fig. 1 which shows the velocity profiles on the central lines. It follows from Fig. 1 that for the isothermal flow:

- the stabilised terms with the parameter ε in (37) does not provide a significant improvement of stability and
- the stability parameter (38) and (40) are almost identical numerically.

Table 1
Maximum and minimum velocities obtained in this computation and [2,12]

Method	u_x − min	u_z − max	u_z − min
1st parameter	−0.3309	0.3047	−0.7472
2nd parameter	−0.3231	0.3194	−0.7518
3rd parameter	−0.3918	0.3460	−0.7760
Ref. [2]	−0.3886	0.3769	−0.5264
Ref. [12]	−0.3829	0.3709	−0.5155

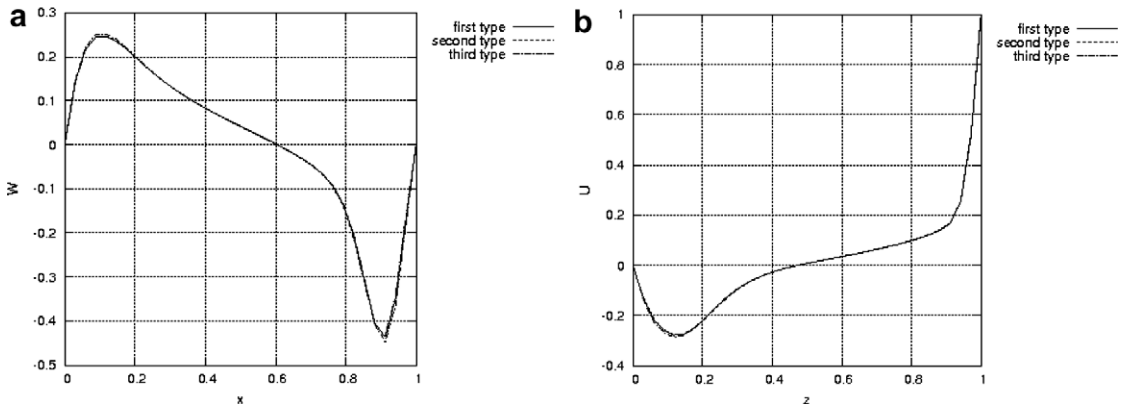

Fig. 1. Flow velocity profiles on central plane of isothermal cavity flow produced by three stabilisation parameters, their deviations based on the first parameter is less than 0.4% (a) normal velocity profile (b) streamwise velocity profile.

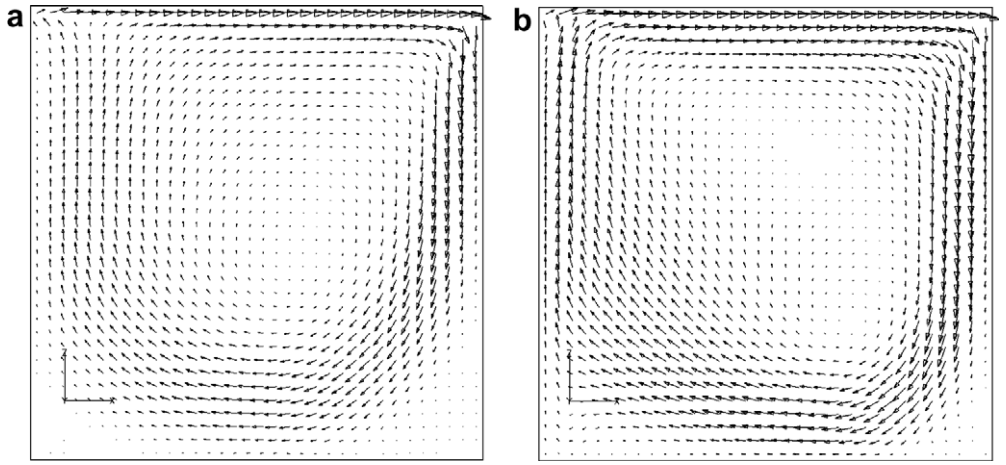

Fig. 2. Comparison of velocity vectors of isothermal and vertically heated cavity flows (a) isothermal flow (b) vertically heated flow.

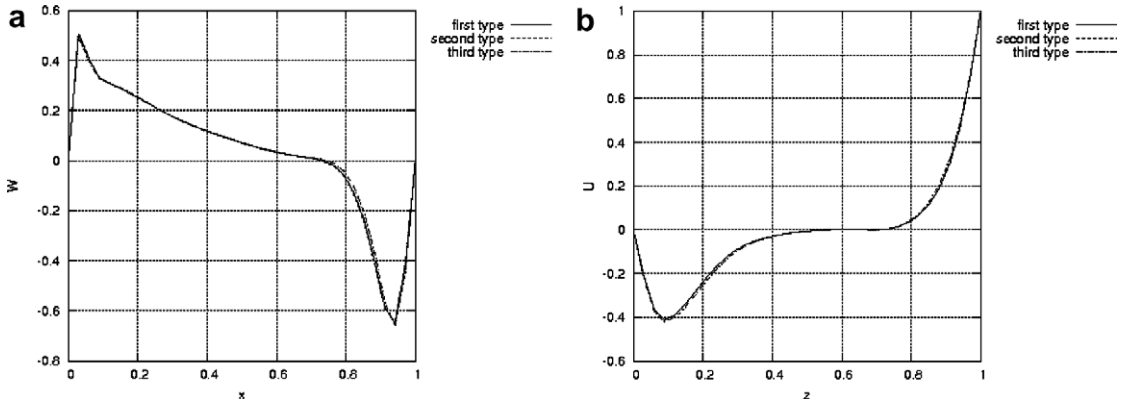

Fig. 3. Flow velocity profiles on central plane of vertically heated cavity flow produced by three stabilisation parameters, their deviations based on the first parameter is less than 1.2% (a) normal velocity profile (b) streamwise velocity profile.

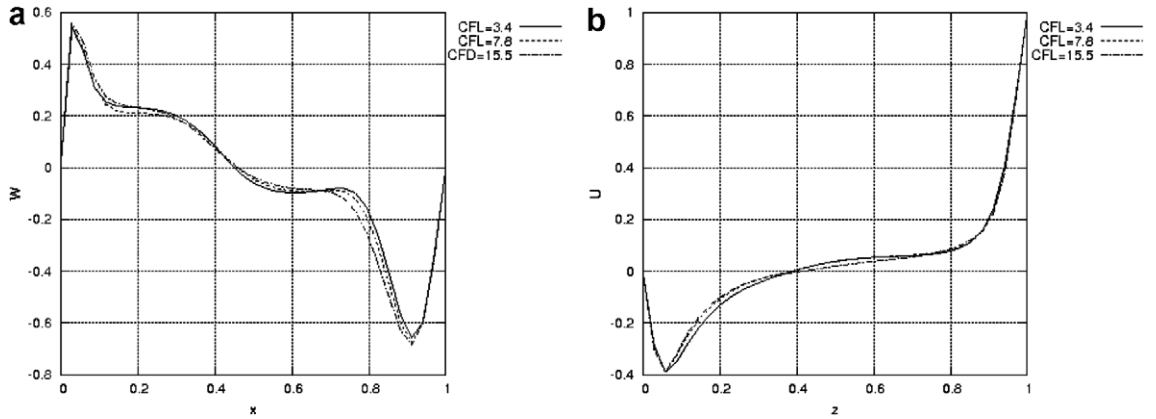

Fig. 4. Flow velocity profiles on central plane at different time step widths (a) normal velocity profile (b) streamwise velocity profile.

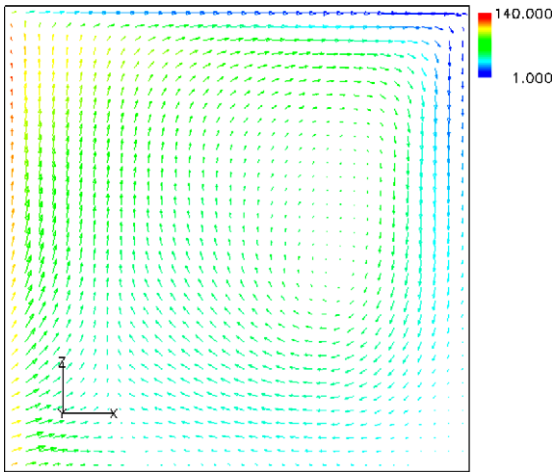

Fig. 5. Velocity vectors at the hot wall with temperature $T = 440$ K. The colour spectrum show the temperature distribution and the figures in the colour bar are relative to the circumstance temperature (300 K).

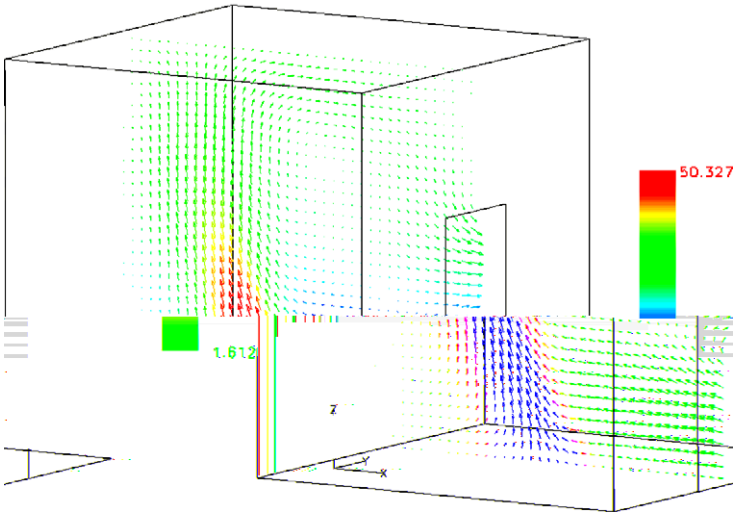

Fig. 6. Flow velocity vectors on the central plane ($y = 1.4$) at instant 150 s, in which the colour spectrum show the temperature distribution and the figures in the colour bar are relative to the circumstance temperature (300 K).

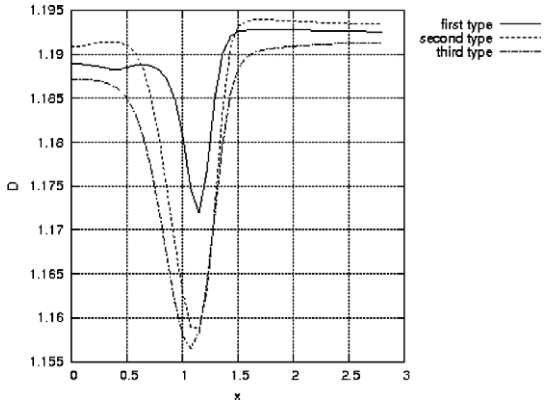

Fig. 7. Air density profiles on central line ($y = 1.4$ and $z = 0.8$) produced by three stabilisation parameters.

4.1.2. Vertical thermal convection

For thermal lid-driven flow, vertical hot wall, as a side wall boundary condition, is maintained at constant temperature $T = 350$ K. Temperature difference between the wall and the gas causes the development of thermal convection. The other boundary conditions in this flow are the same as for the isothermal.

Fig. 2 displays the velocity vectors of the thermal flow and isothermal flow on the cross-section at $y = 0.5$. We may see that the thermal convection leads to the formulation of two vortices; one is upper and one down. To investigate the performance of the numerical schemes, the streamwise and normal velocity profiles are obtained for the three parameters (38)–(40), which is presented in Fig. 3. Again the differences of the computational results by these three parameters (38)–(40) are minor.

It should be pointed out that all the numerical tests in this work have been carried out for CFL number more than one. The influence of the time steps or CFL numbers on computations is presented in Fig. 4. Note that (40) is involved in the time step. One can see that the influence of CFL number is minor. It is found that the proposed numerical schemes allow a very large time step, say $\Delta t = 2$ s in this case, which corresponds to CFL = 75, and produce completely stable computations.

In order to investigate the flow with higher-temperature gradient we reset the hot wall to 440 K. The time step and CFL number for this computation are $\Delta t = 0.4$ s and CFL = 15, respectively. Fig. 5 displays the

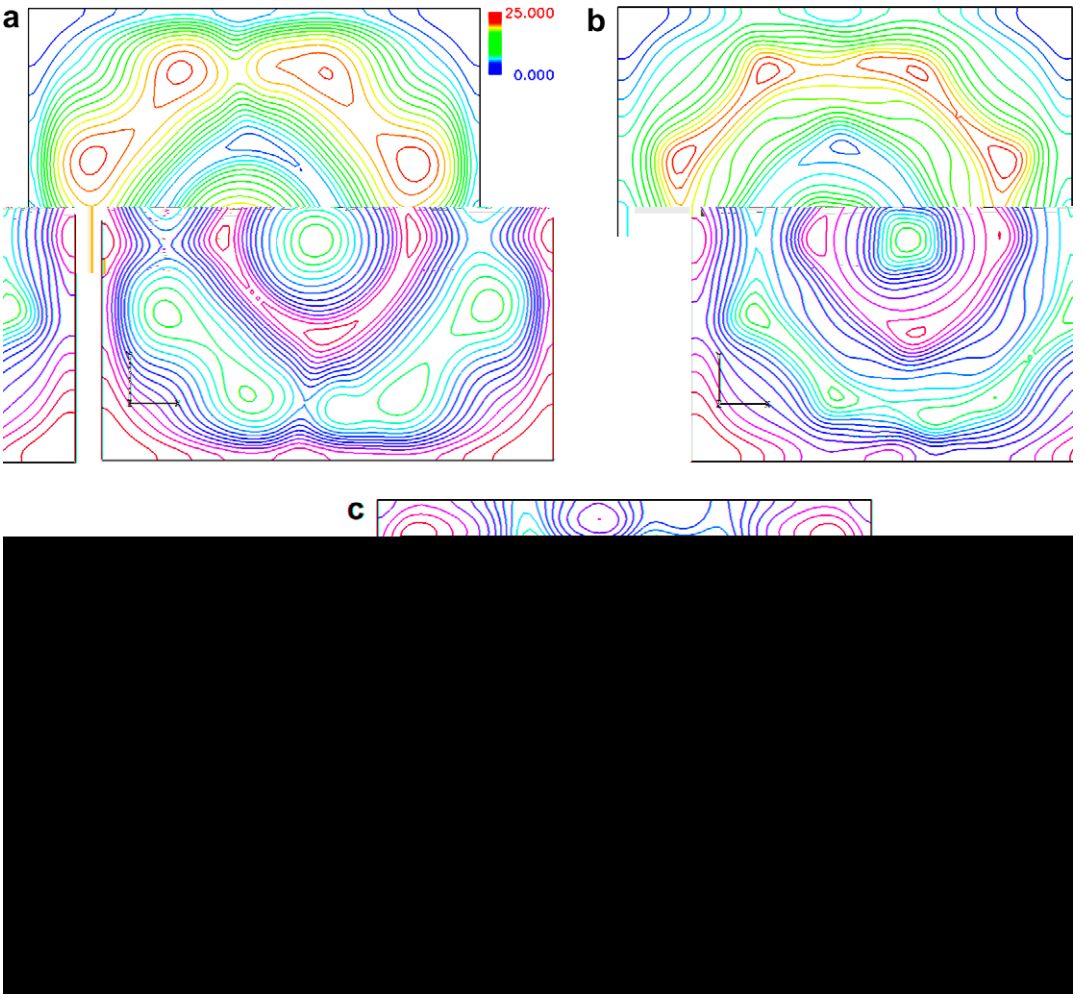

Fig. 8. Temperature contours on planes (a) $z = 0.2l_z$, (b) $z = 0.5l_z$ and (c) $z = 0.8l_z$. The colour spectrum show the temperature distribution and the figures in the colour bar are relative to the circumstance temperature (300 K).

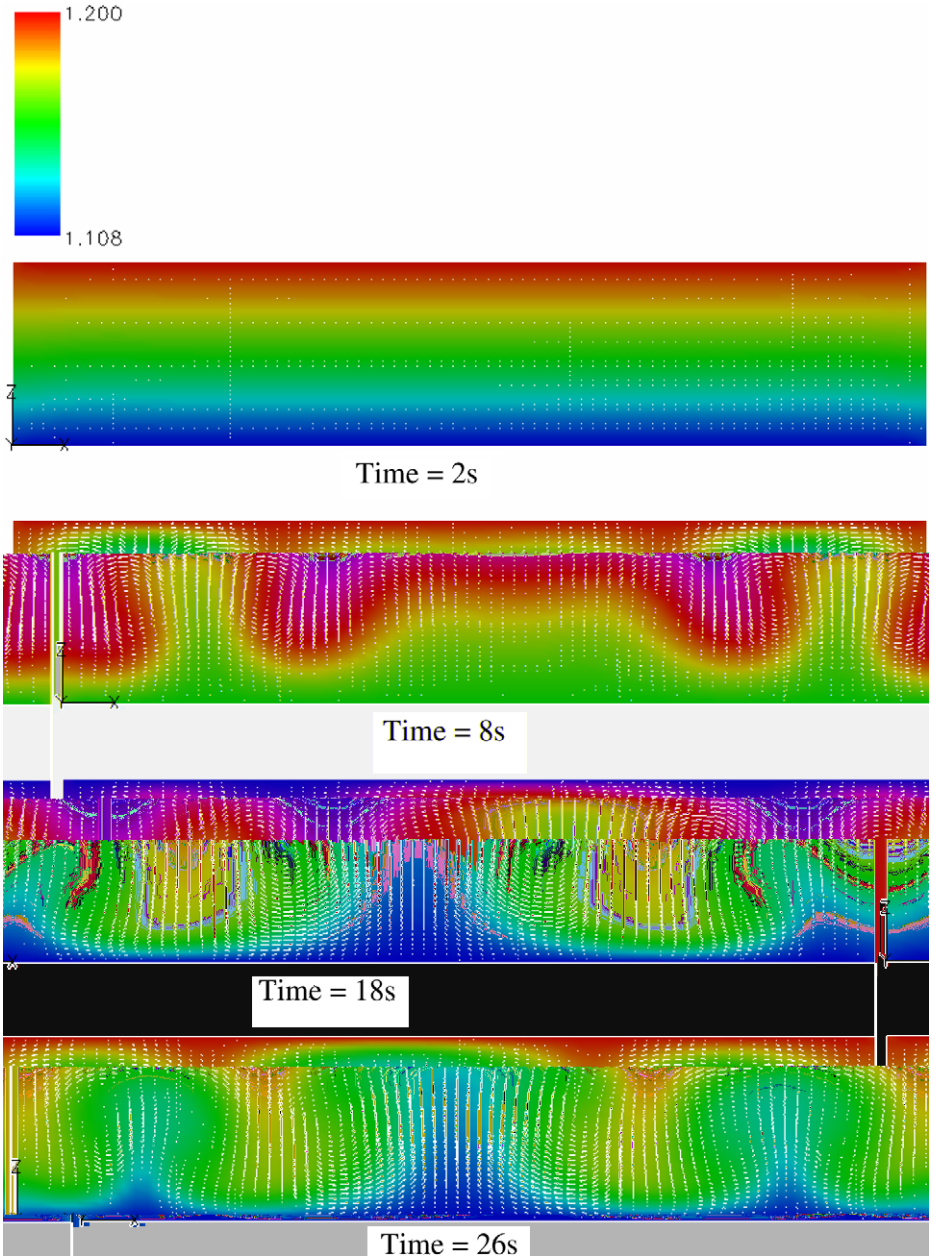

Fig. 9. Evolution of Rayleigh–Benard convection on $y = 0.2l_y$. The background colour spectrum show the density distribution and the vectors present the convection velocities.

velocity vectors on the central section. Comparing it with Fig. 2(b) we can see that the effect of a higher hot wall on the flow is mainly concentrated near the hot wall area.

4.2. Convection in fire compartment

The second numerical test is a compartment fire. The dimension of the compartment is $2.8 \times 2.8 \times 2.18\ \mathrm{m}^3$ (*length* × *width* × *height*) with an open door on the side wall of the room whose dimension is $0.74 \times 1.83\ \mathrm{m}^2$ (length × height). The fire is located at the centre of the room floor that is modelled by a heat

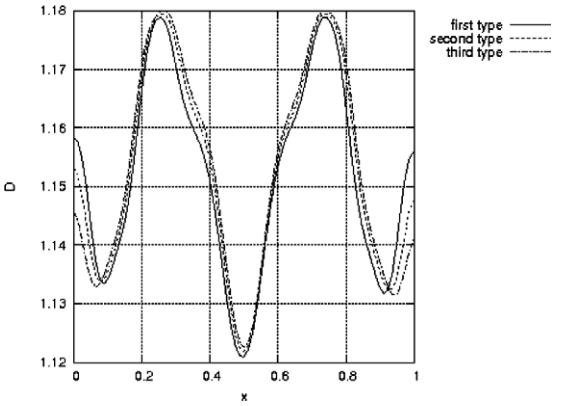

Fig. 10. Air density profiles on central line ($y = 0.5$ and $z = 2.5$) produced by three stabilisation parameters.

source with the heat release rate 5 KW. The compartment is meshed by about 100,000 hexahedral elements. Boundary conditions on the walls, ceiling and floor of the room take into account no-slip velocity and adiabatic conditions. Free boundary condition is imposed on the opening door. Thus the convection is developed due to the heat source in the middle of the floor.

Fig. 6 displays the velocity vectors in the air flow for central section at time instant 150 s. The colour[1] spectrum shows the temperature distribution. One can see that the computation reproduces a low-temperature inflow of air into the compartment in the bottom area of the door and a higher-temperature outflow of combustion products under the door soffit.

In this case study, the tested maximum time steps $\Delta t = 2$ s and maximum CFL number is CFL = 157, under which the computation is still stable. For this problem, we found the three stabilised parameters have different effects on the computational results. For example, Fig. 7 presents the air density distributions on the central line of the compartment produced by the three stabilised parameters. The second and third parameters give the similar solutions, which are quite different from that by the first parameter. This shows that the stability term ε plays more important role for the fire problem with heat sources inside computational domains.

4.3. Rayleigh–Benard flows

Rayleigh–Benard convection is a classic transitional thermal flow. In this section we take it as a case study to test the proposed numerical scheme. The computational domain is 3D rectangular enclosure with geometric aspect ratio: $l_x : l_y : l_z = 5 : 5 : 1$, which is meshed by $50 \times 50 \times 30$ elements. The bottom wall ($z = 0$) is slowly heated to a higher-temperature 320 K initially and the top wall is kept at 300 K. Thus we have a linear temperature profile from the high temperature on the bottom wall to the low-temperature on the top wall. Then the bottom wall is suddenly heated to 325 K. On the side walls adiabatic boundary conditions are used.

The flow structures are controlled by the Rayleigh number $Ra = g l_z^3 \frac{\Delta T}{T_0} \frac{1}{\kappa \nu}$, where $g, l_z, \Delta T, T_0, \kappa$ and ν denote, respectively, the gravity acceleration, height of the computational domain, temperature difference between the bottom and top walls, averaged initial temperature, thermal conductivity and kinematic viscosity. In [23], a similar computation is reported. In order to compare our computations with [23], we choose $Ra = 8 \times 10^3$. Fig. 8 displays the temperature contours at steady state on the cross-section, $z = 0.2 l_z, z = 0.8 l_z$ and $z = 0.5 l_z$. The flow structures produced by this scheme are basically identical with the results from [23, Figs. 5(d), 6(d) and 7(d)]. However we also noticed some difference of both results, in particular in Fig. 8(c). The reason is that the basic Eqs. (10)–(15) we solve are some different from [23]. The development of the convection is shown on Fig. 9; the background colour spectrum displays the density distribution and the arrows denote the convection velocities.

[1] For interpretation of colour in Figs. 5, 6, 8 and 9 the reader is referred to the web version of this article.

In this study, we tested two time steps: a small time step $\Delta t = 0.05$ (CFL = 1.8) and a large time step $\Delta t = 0.5$ (CFL = 18). The small time step is for calculation of the detailed development of Rayleigh–Benard convection (Fig. 9), and the large time step allows the obtaining of the steady state very quickly (Fig. 8).

This numerical test also shows that computational performance of the stabilised parameters is similar to that for the driven cavity flow. The three stability parameters produce almost identical numerical results. For example, Fig. 10 shows density profiles on the central line obtained with the three stabilised parameters.

5. Conclusions

In this paper we have derived an effective implicit finite element scheme to solve a set of equations which govern thermal flow problems at low Mach number. The proposed scheme allows a large time step width. In order to investigate the performance of the proposed method, three representative case studies have been carried out in this work. The numerical tests show that the numerical scheme can produce the accurate numerical solutions to unsteady flows when a small enough time step is used. Moreover for large time step the computation is still robust and stable. This will speed up the computations for steady flows.

There are three stability parameters in the proposed numerical scheme. Theoretically they can be calculated by solving the local problem (36) on each element. In practice, however, they are always obtained by approximations. In this work we tested three stabilising parameters. It is found that they can produce quite similar results for the thermal flows induced by hot boundaries. For inner heat sources the computational results diverge significantly. Therefore the second and third parameters are recommended for the flows with heat internal sources in computational domains.

References

[1] P. Bastian, K. Birken, K. Johannsen, S. Lang, N. Neuss, H. Rentz-Reichert, C. Wieners, UG-a flexible software toolbox for solving partial differential equations, Comput. Visual. Sci. 1 (1997) 27–40.
[2] O. Botella, R. Reyrel, Benchmark spectral results on the lid-driven cavity flow, Comput. Fluids 27 (4) (1998) 421–433.
[3] F. Brezzi, M. Fortin, Mixed and Hybrid Finite Element Methods, Springer-Verlag, Berlin, 1991.
[4] F. Brezzi, L.P. Franca, T.J.R. Hughes, A. Russo, $b = \int g$, Methods Appl. Mech. Eng. 145 (1997) 329–339.
[5] F. Brezzi, D. Marini, A. Russo, Applications of the pseudo residual-free bubbles to the stabilization of convection–diffusion problems, Method Appl. Mech. Eng. 166 (1998) 51–63.
[6] R. Codina, A stabilised finite element method for generalised stationary incompressible flows, Method Appl. Mech. Eng. 190 (2001) 2681–2706.
[7] L.P. Franca, S.L. Frey, Stabilised finite element methods: II. The incompressible Navier–Stokes equations, Method Appl. Mech. Eng. 99 (1992) 209–233.
[8] L.P. Franca, A. Russo, Deriving upwinding, mass lumping and selective reduced integration by residual-free bubble, Appl. Math. Lett. 9 (1996) 83–88.
[9] L.P. Franca, A. Russo, Mass lumping emanating from residual-free bubbles, Method Appl. Mech. Eng. 142 (1997) 353–360.
[10] L.P. Franca, A. Russo, Unlocking with residual-free bubbles, Methods Appl. Mech. Eng. 142 (1997) 361–364.
[11] C. Gatti-Bono, P. Colella, An anelastic all speed projection method for gravitationally stratified flows, J. Comput. Phys. 216 (2006) 589–615.
[12] U. Ghia, K.N. Ghia, C.T. Shin, High Re solution for incompressible flow using the Navier–Stokes equations and a multigrid method, J. Comput. Phys. 48 (1982) 387–411.
[13] T.J.R. Hughes, Multiscale phenomena: Green's functions, the Dirichlet-to-Neumann formulation, subgrid scale models, bubbles and the origins of stabilised methods, Method. Appl. Mech. Eng. 127 (1995) 387–401.
[14] B. Lessani, M.V. Papalexandris, Time-accurate calculation of variable density flows with strong temperature gradient and combustion, J. Comput. Phys. 212 (2006) 218–246.
[15] W. Liu, Modeling of Swirling Turbulent Flows, IHS-Mitteilungen Nr 22, Stuttgart University, 2001.
[16] K.B. McGrattan, H.R. Baum, R.G. Rehm, Fire-driven flows in enclosures, J. Comput. Phys. 110 (1994) 285–291.
[17] Madja, Sethian, The derivation and numerical solution of the equations for zero Mach number combustion, Combust. Sci. Tech. 42 (1985) 185–205.
[18] K.B. McGrattan, H.R. Baum, R.G. Rehm, Large eddy simulations of smoke movement, Fire Safety J. 30 (2) (1998) 161–178.
[19] R.B. Pember, A.S. Almgren, J.B. Bell, P. Colella, L. Howell, M. Lai, A higher-order projection method for simulation of unsteady turbulent nonpremixed combustion in an industrial burner, in: Proc. of the 8th Inter. Symp. on Transport Phenomena in Combus., July 16–20, 1995, San Francisco, CA, USA, or available from: http://seesar.lbl.gov/CCSE/Publications/pub_date.html.
[20] R.G. Rehm, K.B. Baum, The equations of motion for thermally driven, buoyant flows, J. Res. National Bureau Standard 8 (3) (1978) 297–308.

[21] C.C. Rossow, Efficient computation of compressible and incompressible flows, J. Comput. Phys. 220 (2007) 879–899.
[22] E. Schall, C. Viozat, B. Koobus, A. Dervieux, Computation of low Mach thermal flows with implicit upwind methods, Int. J. Heat Mass Transf. 46 (2003) 3909–3926.
[23] Tang, Q. Li, Tsang, T.H. Tate, Temporal, spatial and thermal features of 3-D Rayleigh–Benard convection by a least-squares finite element method, Comput. Methods Appl. Mech. Eng. 140 (1997) 201–219.
[24] I. Teleaga, M. Seaid, I. Gasser, A. Klar, J. Struckmeier, Radiation models for thermal flows at low Mach number, J. Comput. Phys. 215 (2006) 506–525.
[25] T.E. Tezduyar, S. Mittal, S.E. Ray, R. Shih, Incompressible flow computations with stabilised bilinear and linear equal-order-interpolation velocity–pressure elements, Methods Appl. Mech. Eng. 95 (1992) 221–242.
[26] E. Turkel, Preconditioned methods for solving the incompressible and low speed compressible equations, J. Comput. Phys. 72 (1987) 277–298.
[27] E. Turkel, A review of preconditioning methods for fluid dynamics, Appl. Numer. Math. 12 (1993) 257–284.
[28] E. Turkel, Preconditioning techniques in computational fluid dynamics, Ann. Rev. Fluid Mech. 31 (1999) 385–416.